

Article

New Bis-Pyrazole-Bis-Acetate Based Coordination Complexes: Influence of Counter-Anions and Metal Ions on the Supramolecular Structures

Afaf Oulmidi ^{1,2}, Smaail Radi ^{1,*} , Haralampos N. Miras ³ , Nayarassery N. Adarsh ⁴  and Yann Garcia ^{2,*} 

¹ LCAE, Department of Chemistry, Faculty of Sciences, University Mohamed I, BP 524, 60 000 Oujda, Morocco; afafoulmidi.ao@gmail.com

² Institute of Condensed Matter and Nanosciences, Molecular Chemistry, Materials and Catalysis (IMCN/MOST), Université catholique de Louvain, 1348 Louvain-la-Neuve, Belgium

³ School of Chemistry, Joseph Black Building, University of Glasgow, Glasgow G12 8QQ, UK; Charalampos.Moiras@glasgow.ac.uk

⁴ School of Chemical Sciences, Mahatma Gandhi University, Kottayam 686560, Kerala, India; adarshnn@gmail.com

* Correspondence: s.radi@ump.ac.ma (S.R.); yann.garcia@uclouvain.be (Y.G.); Fax: +32-1047-2330 (Y.G.)

Abstract: A new flexible bis-pyrazol-bis-acetate ligand, diethyl 2,2'-(pyridine-2,6-diylbis (5-methyl-1H-pyrazole-3,1-diyl))diacetate (L), has been synthesised, and three coordination complexes, namely, [Zn(L)₂](BF₄)₂ (**1**), [Mn(LCl₂)] (**2**) and [Cd(LCl₂)] (**3**) have been obtained. All ligands and complexes were characterised by IR, mass spectroscopy, thermogravimetric analysis and single-crystal X-ray diffraction. Single crystal X-ray diffraction experiment revealed that the primary supramolecular building block of **1** is a hexagonal chair shaped 0D hydrogen bonded synthon (stabilised by C–H···O hydrogen bonding and C=O···π interactions), which further built into a 2D corrugated sheet-like architecture having a 3-c net honeycomb topology, and finally extended to a 3D hydrogen bonded network structure having a five nodal 1,3,3,3,7-c net, through C–H···F interactions. On the other hand, the two crystallographically independent molecules of **2** exhibited two distinct supramolecular structures such as 2D hydrogen bonded sheet structure and 1D zigzag hydrogen bonded chain, sustained by C–H···O and C–H···Cl interactions, which are further self-assembled into a 3,4-c network structure, and **3** showed a 2D hydrogen bonded sheet structure. The supramolecular structural diversity in these complexes is due to the different conformations adopted by the ligands, which are mainly induced by different metal ions with coordination environments controlled by different anions. Hirshfeld surface analysis was explored for the qualitative and quantitative analysis of the supramolecular interactions.



Citation: Oulmidi, A.; Radi, S.; Miras, H.N.; Adarsh, N.N.; Garcia, Y. New Bis-Pyrazole-Bis-Acetate Based Coordination Complexes: Influence of Counter-Anions and Metal Ions on the Supramolecular Structures. *Sustainability* **2021**, *13*, 288. <https://doi.org/10.3390/su13010288>

Received: 1 December 2020

Accepted: 22 December 2020

Published: 30 December 2020

Publisher's Note: MDPI stays neutral with regard to jurisdictional claims in published maps and institutional affiliations.



Copyright: © 2020 by the authors. Licensee MDPI, Basel, Switzerland. This article is an open access article distributed under the terms and conditions of the Creative Commons Attribution (CC BY) license (<https://creativecommons.org/licenses/by/4.0/>).

Keywords: organic synthesis; coordination chemistry; single crystal X-ray diffraction; Hirshfeld surface analysis

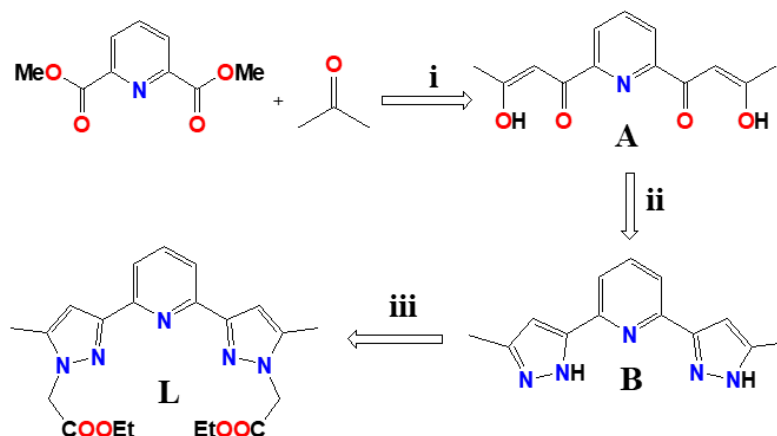
1. Introduction

Designing coordination complexes by using supramolecular self-assembly is an important research area in materials chemistry [1]. The use of relatively simple organic ligands and metal ions through their kinetically labile and thermodynamically stable coordination bonds attracted many research groups due to their various potential applications [2–7]. Such self-assembly resulted in channels or void spaces, wherein host-guest chemistry played a role for the incorporation of small molecules or anions within such empty spaces [8]. In most of the coordination complexes so far reported, the ligands having only one hetero nitrogen as the donor atom such as pyridine [9], picoline [10], isoquinoline [11] etc. were used. On the other hand, ligands having two hetero nitrogen atoms such as imidazole [12], pyrazole [13,14] and pyrazine [15] are not much explored in the coordination chemistry of transition metals.

Our research group has recently started a research programme on coordination complexes built from pyrazole ligands. For example, we have reported the crystal structures of Co(II)/Cu(II) coordinated complexes of pyrazole-dicarboxylate acid ligand and established their supramolecular structures [16]. In another work, we have demonstrated the effect of the aliphatic backbone of the bis-pyrazole-bis-carboxylate ligand on the supramolecular structures of their Co(II)/Cu(II)/Cd(II) coordination complexes [17]. In a further account, we have studied the effect of anions and hydrogen bonding on the supramolecular structural diversities of Cu(II) and Mn(II) coordination complexes obtained from a novel bis-pyrazole ligand [18]. More recently, two new pyrazole-acetamide ligands and their solid-state structures of coordination complexes characterised by their remarkable antioxidant activity have been reported too, in the context of the effect of hydrogen bonding on the self-assembly process [19]. Last but not least, we have reported the crystal structure–bioactivity correlation of three mononuclear coordination complexes of a pyrazolyl-benzimidazole ligand [20].

In the present study, we aim to explore the effect of ligating topologies, counter anions and the metal ion nodes on the supramolecular structures of coordination complexes obtained from a conformationally flexible bis-pyrazol-bis-acetate ligand having a pyridine backbone (Scheme 1), namely diethyl 2,2'-(pyridine-2,6-diylbis(5-methyl-1H-pyrazole-3,1-diyl)) diacetate (**L**) because of the following reasons:

- (1) The ligand **L** is an *N*-heterocyclic tridentate pyrazolyl pyridine compound capable of forming various coordination modes, and ligating topology with transition metal ions [21].
- (2) This type of pyridine ligand having pyrazolyl groups at the second and sixth position, possesses a wide range of interesting chemical and/or physical properties, such as catalytic [22,23], electrochemical [24], magnetic and photophysical properties [25].
- (3) Many coordination complexes containing both Lewis base donors and Lewis acid acceptors in the same ligand [26] such as 2,6-bis(pyrazolyl) pyridine have been reported [23–27] according to the Hard-Soft acid base theory [28].
- (4) **L** is a new ligand, not yet reported.

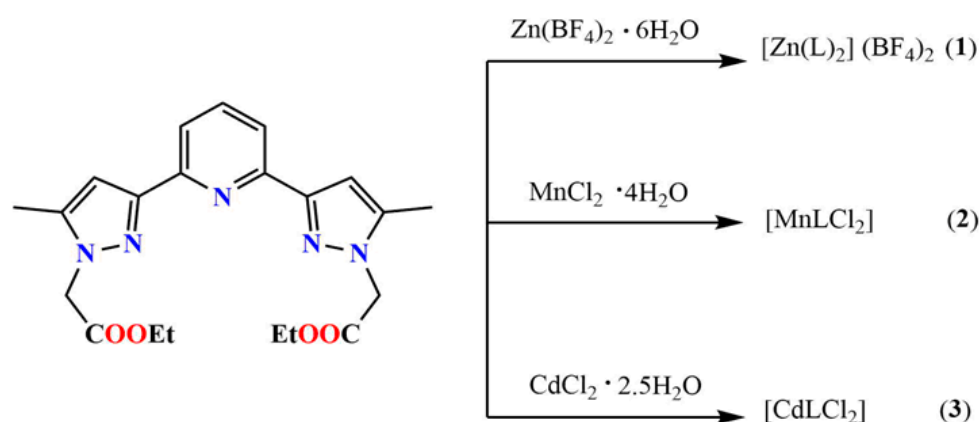


Scheme 1. Synthesis of ligand **L**. (i) MeONa, THF, reflux. (ii) MeOH, $\text{NH}_2\text{-NH}_2$ / H_2O , reflux. (iii) NaH, $\text{BrCH}_2\text{COOEt}$, THF, reflux.

In this work, we shall investigate the coordination properties of **L** with Zn(II), Mn(II) and Cd(II), which are recognised non-biodegradable and toxic metal ions, toxic for both health and environment. For this purpose, we have reacted **L** with $\text{Zn}(\text{BF}_4)_2 \cdot 6\text{H}_2\text{O}$, $\text{MnCl}_2 \cdot 4\text{H}_2\text{O}$ and $\text{CdCl}_2 \cdot 2.5\text{H}_2\text{O}$ in a 1:2 molar ratio, which led to single crystals which were systematically investigated by single crystals X-ray diffraction (Scheme 2).

The crystal structures of three coordination complexes were discussed in the context of their effect of conformation dependent ligating topology, counter anions and metal ion nodes on the supramolecular structural diversities. We have also present, for completeness,

the crystal structure of the ligand **L** and of the intermediate compound 2-(5-methyl-1H-pyrazol-3-yl)-6-(3-methyl-1H-pyrazol-5-yl) pyridine **B** (See Scheme 1).



Scheme 2. Schematic representation of the synthesis of coordination complexes **1**, **2** and **3**.

2. Materials and Methods

All solvents and chemicals, obtained from usual commercial sources, were of analytical grade and used without further purification. ^1H and ^{13}C NMR spectra were obtained on a Bruker AC 300 MHz spectrometer with the solvent proton peak as internal standard. High resolution mass spectrometry HRMS data were obtained with a Q Exactive ThermoFisher Scientific ion trap spectrometer by using ESI ionisation. FT-IR spectra were recorded with KBr discs on a Perkin Elmer 1310 spectrometer. Thermogravimetric Analyses (TGA) were carried out on a Mettler Toledo TGA/SDTA 851e analyser by loading 3–4 mg of sample, and the mass loss was monitored under nitrogen on warming from room temperature to 900 °C at 10 °C/min.

A suitable single crystal was selected and mounted onto a rubber loop using Fomblin oil. Single-crystal X-ray diffraction (SXRD) data of **B**, **L**, **1**, **2**, **3** were recorded on a Bruker Apex CCD diffractometer (λ (MoK_α) = 0.71073 Å) at 150 K equipped with a graphite monochromator. Structure solution and refinement were carried out with SHELXS-97 [29] and SHELXL-97 [30] using the WinGX software package [31]. Data collection and reduction were performed using the Apex2 software package. Corrections for the incident and diffracted beam absorption effects were applied using empirical absorption corrections [32]. All the non-H atoms were refined anisotropically. The positions of hydrogen atoms were calculated based on stereochemical considerations using the riding model. Final unit cell data and refinement statistics for **B**, **L**, **1**, **2**, **3** are collected in Table 1.

Synthesis of Ligands and Coordination Complexes

(2Z,2'Z)-1,1'-(pyridine-2,6-diyl)bis(3-hydroxybut-2-en-1-one) (**A**)

To a mixture of dimethyl pyridine-2,6-dicarboxylate (3 g, 15.37 mmol) solubilised in anhydrous THF (50 mL) freshly prepared sodium methanoate (3.32 g, 61.48 mmol) was added, then 2.27 mL (30.74 mmol) of acetone were slowly added at 0 °C. After reflux for 4 h, the mixture was filtered and the precipitated product was washed with diethyl ether (30 mL) and then dried in a desiccator. This salt was neutralised in water (30 mL) by adding diluted glacial acetic acid until pH = 5.5. The yellow precipitated was filtered off, washed with water (20 mL) and dried in a desiccator. Yield: 3.2 g (52%).

M. p. 77(1) °C

FTIR [KBr disk, ν (cm^{-1})] = 792 (s), 1086 (m), 1428 (m), 1567 (s), 2363 (w), 3384 (m).

ESI: m/z = 248.09 $[\text{M} + \text{H}]^+$ for $\text{C}_{13}\text{H}_{14}\text{O}_4\text{N}$ in MeOH.

^1H NMR [300 MHz, CDCl_3 , 298 K, δ (ppm)] 2.29 (s, 6H, $\text{CH}_3\text{-C}$); 4.36 (s, 2H, C-OH); 6.97 (s, 2H, C=CH); 8.21 (m, 3H, pyridine)

^{13}C NMR [300 MHz, CDCl_3 , 298 K, δ (ppm)] 26.31 (2C, $\text{CH}_3\text{-C}$); 97.42 (2C, $\text{C}=\text{C}$); 124.47 (2C, pyridine); 138.34 (1C, pyridine); 151.88 (2C, $\text{C}_{\text{pyridine-N}}$); 180.58 (2C, $\text{C}=\text{O}$); 195.14 (2C, C-OH)

2-(5-methyl-1H-pyrazol-3-yl)-6-(3-methyl-1H-pyrazol-5-yl) pyridine (**B**)

A mixture of diketone (**A**) (2.21 g, 89.38 mmol) and an excess of hydrazine monohydrate (1.56 g, 31.16 mmol) were heated under reflux in 20 mL of methanol for 18 h. After cooling to room temperature, the mixture was concentrated to reduce the solvent, and water (50 mL) was added to the mixture. The resulting white solid was filtered and washed with H_2O (20 mL). The obtained product was recrystallised in a mixture (20 mL) of dichloromethane/methanol (1/1) to give white crystals. Yield 1.38 g (64%).

M. p. 211(1) °C

FTIR [KBr disk, $\nu \text{ cm}^{-1}$] = 819 (s), 1031 (s), 1450 (s), 1580 (s), 1575 (m), 3133 (w), 3217 (w).

ESI: $m/z = 240.12$ [$\text{M} + \text{H}$] $^+$ for $\text{C}_{13}\text{H}_{14}\text{N}_5$ in MeOH.

^1H NMR [300 MHz, DMSO, 298 K, δ (ppm)] 2.26 (m, C-CH_3); 6.73 (s, 1H, $\text{C}=\text{CH}$); 6.65 (s, 1H, $\text{C}=\text{CH}$); 7.64 (m, 3H, pyridine) 12.67 (s, 1H, N1Hpyrazolyl) 13.05 (s, N2 Hpyrazolyl).

^{13}C NMR [300 MHz, DMSO, 298 K, δ (ppm)] 10.95 (1C, $\text{CH}_3\text{-Pyz}$); 14.03 (1C, $\text{CH}_3\text{-Pyz}$); 102.92 (1C, CH-Pyz); 103.44 (1C, CH-Pyz); 117.73 (1C, pyridine); 118.45 (1C, pyridine); 139.87 (2C, C-NHPyz); 142.17 (1C, Pyridine); 148.99 (2C, $\text{Cpyrazol}=\text{N}$); 152.14 (1C, Pyridine).

Diethyl 2,2'-(pyridine-2,6-diylbis(5-methyl-1H-pyrazole-3,1-diyl)) diacetate (**L**)

A mixture of (**B**) (4.2 mmol) and sodium hydride (16.7 mmol) in tetrahydrofuran (80 mL) was refluxed for 2 h. After cooling to 0 °C, a solution of ethyl bromoacetate (8.35 mmol) in tetrahydrofuran (20 mL) was slowly added. The reaction mixture was heated under reflux for 3 days, then filtered and the solvent was evaporated to dryness. The obtained residue was precipitated by addition of diethyl ether (30 mL) at 0 °C, and the resulting solid was filtered and washed with Et_2O (20 mL). The isolated product was purified on silica using dichloromethane and methanol (9:1) to give a white pure product. Yield: 0.70 g (41%). This product was crystallised in dichloromethane to obtain colourless crystals.

M. p. 165(1) °C

FTIR [KBr disk, $\nu \text{ cm}^{-1}$] = 792 (s), 1028 (s), 1270 (m), 1436 (m), 1569 (s), 1741 (s), 2996 (w)

ESI-MS: $m/z = 412.197$ [$\text{M} + \text{H}$] $^+$ for $\text{C}_{21}\text{H}_{26}\text{O}_4\text{N}_5$ in MeOH

^1H NMR [300 MHz, CDCl_3 , 298 K, δ (ppm)] 1.27 (t, 6H, $\text{CH}_3\text{-CH}_2$); 2.32 (s, 6H, $\text{CH}_3\text{-C}$); 4.22 (q, 4H, $\text{CH}_2\text{-CH}_3$); 4.90 (s, 4H, $\text{CH}_2\text{-C}=\text{O}$); 6.84 (s, 1H, CH pyrazolyl); 7.78 (m, 3H, pyridine).

^{13}C NMR [300 MHz, CDCl_3 , 298 K, δ (ppm)] 11.32 (2C, $\text{CH}_3\text{-Pyz}$); 14.27 (2C, $\text{CH}_3\text{-CH}_2$); 51.20 (2C, $\text{CH}_2\text{-NPyz}$); 61.95 (2C, $\text{CH}_2\text{-O}$); 105.30 (2C, CH-Pyz); 118.73 (2C, pyridine); 137.24 (2C, C-NPyz); 140.88 (1C, Pyridine); 151.60 (4C, $\text{Cpy} = \text{C}$, Cpy-Cpyz) 167.86 (2C, $\text{C}=\text{O}$).

$[\text{Zn}(\text{L})_2](\text{BF}_4)_2$ (**1**)

41 mg of **L** (0.1 mmol, 2 eq.) was dissolved in methanol (10 mL). To this solution was added a methanolic solution (5 mL) of 12 mg (0.05 mmol, 1 eq.) of $\text{Zn}(\text{BF}_4)_2 \cdot 6\text{H}_2\text{O}$. The reaction mixture was stirred for 15 min. Colourless crystals suitable for X-ray analysis were obtained by vapour diffusion of diethyl ether into the reaction mixture after ten days. Yield: 0.021 g (48%).

FTIR (KBr disk) $\nu \text{ cm}^{-1}$: 2992 (m), 1579 (w), 1414 (w), 1232 (m), 1082 (m), 1026 (w), 829 (w).

ESI-MS: $m/z = 817.33$ [$\text{M-COOEt} + \text{H}$] $^+$ for $\text{C}_{39}\text{H}_{47}\text{N}_{10}\text{O}_6\text{Zn}$ in DMF.

^1H NMR [300 MHz, DMSO, 298 K, δ (ppm)] 1.23 (t, 6H, $\text{CH}_3\text{-CH}_2$); 2.28 (s, 6H, $\text{CH}_3\text{-C}$); 4.12 (q, 4H, $\text{CH}_2\text{-CH}_3$); 5.90 (s, 4H, $\text{CH}_2\text{-C}=\text{O}$); 6.75 (s, 1H, CH pyrazolyl); 7.76 (m, 3H, pyridine)

$[\text{MnLCl}_2]$ (**2**)

41 mg (0.10 mmol, 2 eq.) of **L** was dissolved in hot methanol (5 mL). To this solution was added a methanolic solution (10 mL) of 98 mg (0.05 mmol, 1 eq.) of $\text{MnCl}_2 \cdot 4\text{H}_2\text{O}$. After stirring for 15 min the resulting solution was left at room temperature. Colourless single crystals were obtained by slow evaporation of the reaction mixture over a period of 1 week. Yield 0.0101 g (40%).

FTIR (KBr disk) ν cm^{-1} : 2981(w), 1747 (s), 1504 (m), 1426 (m), 1232 (m), 1013 (m), 819 (w).

ESI-MS: $m/z = 501.097$ $[\text{M} + \text{H}]^+$ for $\text{C}_{21}\text{H}_{26}\text{O}_4\text{N}_5\text{Mn}$ in DMF.

$[\text{CdLCl}_2]$ (**3**)

41.1 mg **L** (0.10 mmol, 2 eq.) was dissolved in MeOH (5 mL). 11.4 mg $\text{CdCl}_2 \cdot 2.5\text{H}_2\text{O}$ (0.05 mmol, 1 eq.) was dissolved with a solution of H_2O (3 mL) and MeOH (3 mL) and added to the above solution of **L**. The resulting solution was filtered and left undisturbed at r.t. After a few days the formed precipitate was recrystallised in CH_3CN (15 mL). White single crystals were obtained by slow evaporation of the reaction mixture over a period of 7 days. Yield 0.007 g (26%).

FTIR (KBr disk) ν cm^{-1} : 2985 (w), 1760 (s), 1508 (m), 1426 (m), 1235 (m), 1021 (w), 806 (w).

ESI-MS: $m/z = 560.061$ $[\text{M} - \text{Cl} + \text{H}]^+$ for $\text{C}_{21}\text{H}_{26}\text{O}_4\text{N}_5\text{Cd}$ in DMF.

3. Results

3.1. Synthesis, FT-IR and UV-Visible Spectroscopy

The ligand **L** was synthesized by following a three-step reaction, in which the dimethyl pyridine-2,6-dicarboxylate was converted to an intermediate compound bis-hydroxy-bis-one (**A**) following a nucleophilic reaction with acetone and NaOMe, in the first step, and in the second step, the intermediate compound was treated by hydrazine hydrate resulting in 2-(5-methyl-1H-pyrazol-3-yl)-6-(5-methyl-2H-pyrazol-3-yl)-pyridine (**B**). In the final step, the reaction of **B** with NaH and $\text{BrCH}_2\text{COOEt}$ lead to the formation of the ligand **L** (Scheme 2) in reasonable yield. The coordination complexes $[\text{Zn}(\text{L})_2](\text{BF}_4)_2$ (**1**), $[\text{MnLCl}_2]$ (**2**) and $[\text{CdLCl}_2]$ (**3**) were synthesised by reacting the ligand **L** with $\text{Zn}(\text{BF}_4)_2 \cdot 6\text{H}_2\text{O}$, $\text{MnCl}_2 \cdot 4\text{H}_2\text{O}$ and $\text{CdCl}_2 \cdot 2.5\text{H}_2\text{O}$, respectively in 1:2 metal/ligand stoichiometric ratio.

The resultant needle shaped crystals were characterised by using FT-IR, UV-visible spectroscopy, electrospray ionisation mass spectrometry (ESI-MS) and SXRD. More detail explanation of FT-IR and UV-visible spectroscopy are given in the SI.

3.2. Crystal Structures

The crystal data of **B**, **L**, **1**, **2** and **3** are given in Table 1. Needle-type crystals were obtained by slow evaporation of dichloromethane and methanol in the case of **L** and a mixture of dichloromethane and ethanol in the case of the ligand **B**. Not surprisingly, the crystal structure of **B** contains an ethanol molecule, whereas no solvent was detected for **L**. Single crystal X-ray diffraction analysis of ligand **B** revealed that the ligand crystallises in the orthorhombic space group $\text{P}2_12_12_1$, which is an achiral member of the Sohncke family defining chiral crystals (Figure 1). The asymmetric unit is composed of one molecule of each **B** and lattice included ethanol. The solvent ethanol was found to be disordered over two positions. In the unit cell, four molecules of ligand and ethanol were present. The N–N bond distances are in the range of 1.343(4)–1.350(4) Å, which is characteristic for pyrazole [20]. From the crystal structure, it is found that the ligand exists as slightly non-planar, in which the planes of the pyrazole rings showed a difference in the angle of 8.68° (a). The ligand **B** undergoes supramolecular self-assembly through N–H \cdots N hydrogen bonding [$\text{N} - \text{H} \cdots \text{N} = 2.887(4)$ Å, $\angle \text{N} - \text{H} - \text{N} = 167^\circ$] interactions comprising the pyrazole functionality, resulting in a P-helix along 2_1 screw axis. Four units of the ligand complete one helical turn with a helical pitch of 21.5 Å. Interestingly, lattice included ethanol molecules were located along the 2_1 screw axis of the helix and are involved in bifurcated hydrogen bonding [$\text{N} - \text{H} \cdots \text{O} = 2.761(8) - 2.866(16)$ Å, $\angle \text{N} - \text{H} - \text{O} = 162 - 173^\circ$] and Van der Waals interactions [3.062(8) Å] with N atoms of pyrazole and pyridine functionalities, respectively (Figure 1b). In the crystal structure, P-helix was additionally stabilised by the adjacent helices with the support of various Van der Waals interactions (Figure 1c–e).

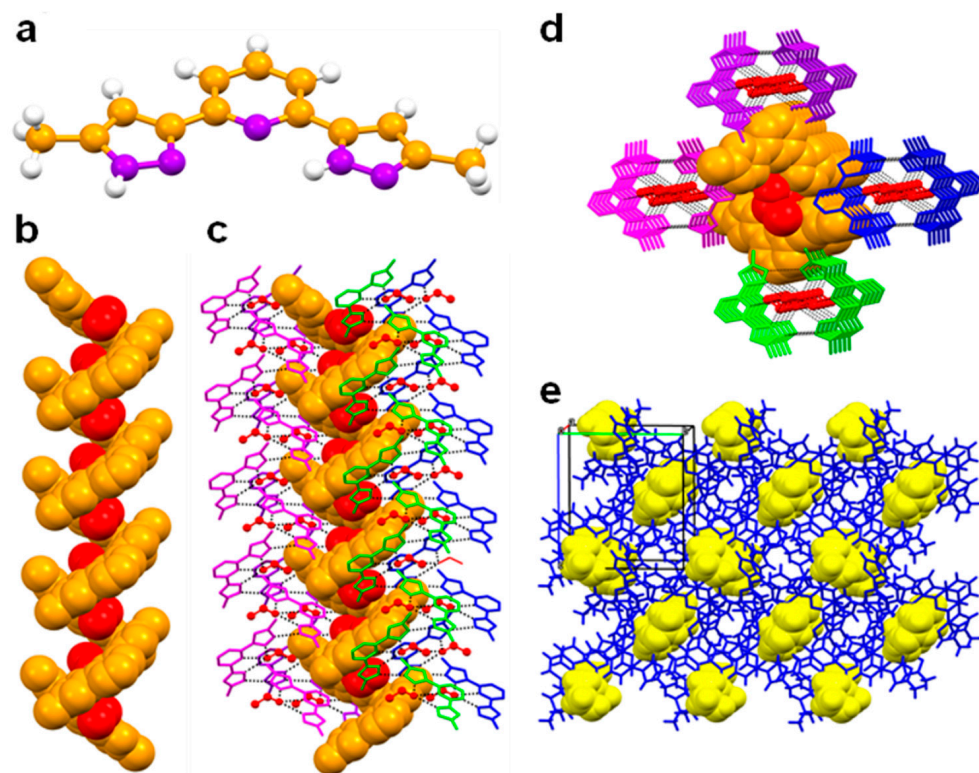


Figure 1. Crystal structure illustration of B—(a) The crystal structure of B (colour code: C—orange, N—purple, H—white); (b) P-helix along the 2_1 screw axis (orange colour spacefill model), displaying the inclusion of ethanol molecules (red colour spacefill model); (c) parallel packing of the M-helices along 2_1 screw axis; (d) along crystallographic axis ‘a’ (adjacent M-helices are shown in purple, blue, magenta, green, in capped stick model); (e) overall packing of M-helices (blue colour capped stick model), displaying the inclusion of ethanol (yellow colour spacefill model).

The chirality obtained from 2-fold rotational axes as a result of the molecular assemblies in the crystal lattice of an achiral component is an important topic in crystal engineering [33]. On the other hand, the ligand L crystallised in the centrosymmetric triclinic space group P-1. The asymmetric unit contains only one molecule of L, and there were two such molecules found in the unit cell, both related to each other by a centre of inversion symmetry. As expected, the ligand showed non-planar structure, which is revealed from the angle between the pyrazole rings (14.13°). Among various plausible conformations, the ligand L showed anti-anti-syn-anti-anti conformation in the crystal structure (Scheme S1). The N–N bond distance was in the range of 1.358(4)–1.350(4) Å, which is the characteristic N–N bond length for pyrazole [20]. Moreover, the C=O, C–O and O–C bond lengths were in the range of 1.184(4)–1.206(8) Å, 1.318(5)–1.319(9) Å and 1.446(5)–1.458(8) Å, respectively [34], which confirms the presence of ethyl acetate functionality in L.

We are interested in the final supramolecular structure of this new ligand L, in which three distinct functionalities such as pyridine, pyrazole and ethyl acetate are present. The C=O of the ester moiety showed hydrogen bonding interaction with the $-\text{CH}_2-$ spacer between the pyrazole and ester moieties via $\text{C}-\text{H}\cdots\text{O}$ hydrogen bonding [$\text{C}-\text{H}\cdots\text{O} = 3.142(5)\text{--}3.281(10)$ Å, $\angle\text{C}-\text{H}-\text{O} = 131\text{--}151^\circ$] lead to the formation of a zero dimensional (0D) synthon, which is further extended through $\text{C}-\text{H}\cdots\text{O}$ interactions into a two dimensional (2D) hydrogen bonded sheet structure through the same $\text{C}-\text{H}\cdots\text{O}$ interaction. Two such sheets are assembled each other through $\text{C}-\text{H}\cdots\text{N}$ hydrogen bonding [$\text{C}-\text{H}\cdots\text{N} = 3.562(6)$ Å, $\angle\text{C}-\text{H}-\text{N} = 166^\circ$] involving a $-\text{CH}_2-$ spacer and the pyrazole N atom leading to the formation of a network structure having Schläfli symbol $\{4^8.6^2\}$ and exhibiting a 5-c net unimodal topology [35]. In fact, such hydrogen bonding resulted in the formation of an

eight-membered hydrogen bonded macrocycle of graph set $R_2^2(8)$. Such pairs of 2D sheets are further self-assembled through weak van der Waals force (Figure 2).

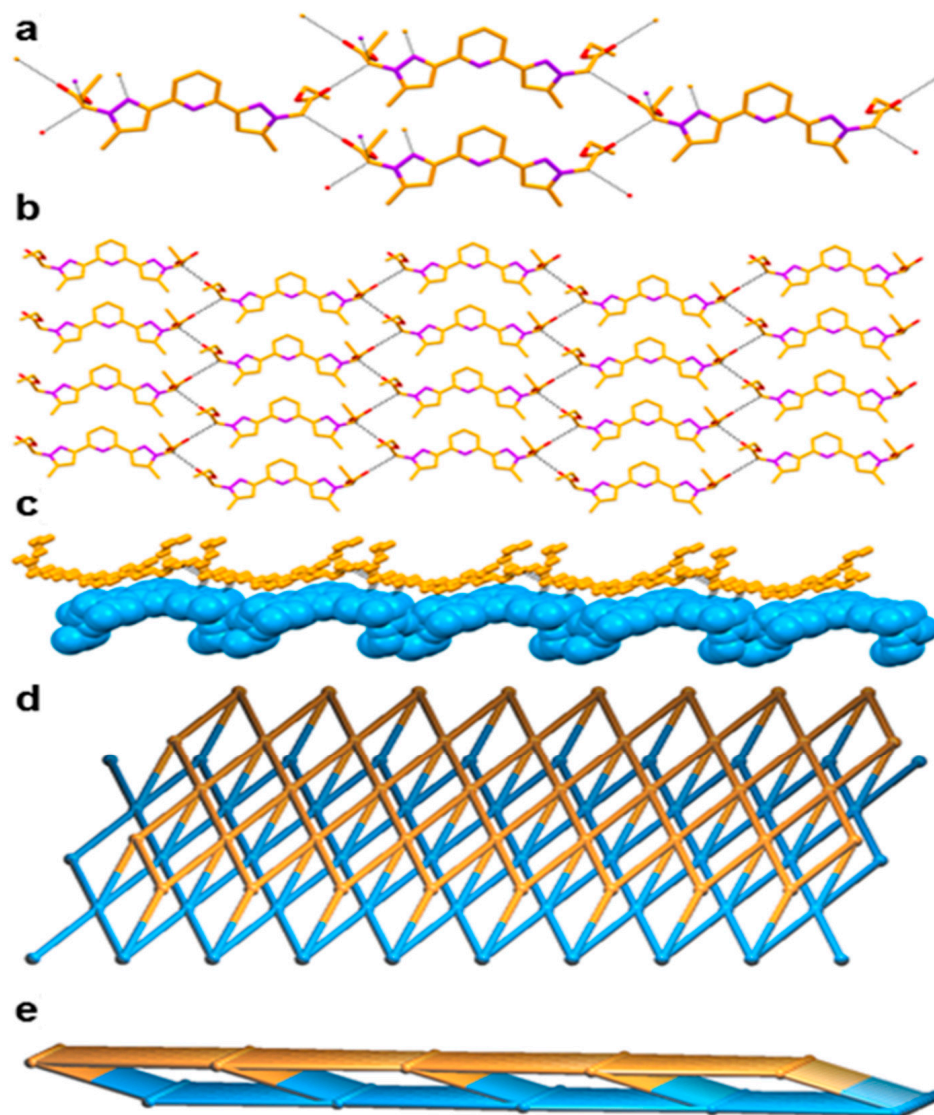


Figure 2. Crystal structure illustration of L—(a) 1D chain; (b) 2D hydrogen bonded sheet structure (colour codes: C—orange, O—red, N—purple); (c) A pair of self-assembled 2D hydrogen bonded sheets (individual sheets are shown in orange and cyan); (d,e) TOPOS [31,35] view of a pair of self-assembled 2D hydrogen bonded sheets, along crystallographic axis 'b' and 'c'.

The asymmetric units of the coordination complexes are shown in Figure 3. A colourless needle-shaped single crystal of **1** crystallised in the centrosymmetric monoclinic space group $P2_1/c$. The asymmetric unit contains two molecules of Zn(II) coordination complex, and four counter anions of tetrafluoroborate (BF_4^-). The metal centre Zn(II) exhibited distorted octahedral geometry [$\angle\text{N-Zn-N} = 74.27(9)\text{--}99.10(10)^\circ$] wherein all of the six coordination sites were occupied by the N atoms (both pyridine and pyrazole) of two molecules of the ligand L.

Table 1. Crystallographic and refinement data for the reported structures.

	B	L	1	2	3
Formula	C ₁₅ H ₁₉ N ₅ O	C ₂₁ H ₂₅ N ₅ O ₄	C ₄₂ H ₅₀ B ₂ F ₈ N ₁₀ O ₈ Zn	C ₂₁ H ₂₅ Cl ₂ MnN ₅ O ₄	C ₂₁ H ₂₅ CdCl ₂ N ₅ O ₄
M _r	285.35	411.46	1061.91	537.30	594.76
T [K]	293(2)	297(2)	150(2)	150(2)	150(2)
γ [Å]	0.71073	0.71073	0.71073	0.71073	0.71073
Crystal system	Orthorhombic	Triclinic	Monoclinic	Monoclinic	Monoclinic
Space group	P2 ₁ 2 ₁ 2 ₁	P-1	P2 ₁ /c	P2 ₁ /c	P2/n
a [Å]	9.036(1)	6.687(1)	22.848(6)	21.183(5)	11.785(3)
b [Å]	12.456(1)	11.333(4)	29.051(7)	18.572(5)	9.296(2)
c [Å]	13.962(1)	15.576(3)	14.640(4)	12.688(3)	11.852(3)
α [°]	90	71.24(2)	90	90	90
β [°]	90	79.22(1)	91.163(4)	100.812(3)	110.813(2)
γ [°]	90	74.17(1)	90	90	90
V [Å ³]	1571.6(3)	1069.0(5)	9715(4)	4903(2)	1213.7(5)
Z	4	2	4	8	2
ρ _c [g cm ⁻³]	1.206	1.278	1.452	1.456	1.627
μ [mm ⁻¹]	0.080	0.091	0.597	0.793	1.157
F(000)	608	436	4384	2216	600
θ range	3.26–24.94	2.90–25.24	2.18–24.96	2.24–26.03	2.86–26.44
Independent reflns	2838	3817	20,039	10,094	2513
Abs. correction	Multi-scan	Multi-scan	Empirical	Empirical	Empirical
Refinement method	Full-matrix least-squares on F ²				
GoF on F ²	1.094	1.097	1.020	1.063	1.079
Final R indices [I > 2 σ(I)]	R ₁ = 0.0510 wR ₂ = 0.1211	R ₁ = 0.087 wR ₂ = 0.1770	R ₁ = 0.0518 wR ₂ = 0.1303	R ₁ = 0.0715 wR ₂ = 0.1539	R ₁ = 0.0264 wR ₂ = 0.0709
R indices (all data)	R ₁ = 0.0607 wR ₂ = 0.1276	R ₁ = 0.1283 wR ₂ = 0.1992	R ₁ = 0.0779 wR ₂ = 0.1448	R ₁ = 0.1008 wR ₂ = 0.1752	R ₁ = 0.0295 wR ₂ = 0.0730

In contrast to the anti-anti-syn-anti-anti conformation of the ligand (non-coordinated to the metal centre), the metal bound ligand **L** molecules showed two distinct conformations such as syn-syn-syn-syn-syn and syn-syn-syn-syn-anti in the coordination complex **1**, with substantial molecular non planarity, which is evident from the corresponding dihedral angles of 9.00–15.77° involving the terminal pyrazole rings. The crystallographically independent molecules of **1**, showed weak C–H···O hydrogen bonding [C–H···O = 3.243(5)–3.307(4) Å, <C–H–O = 117–128°] involving C–H of pyridine and C=O of the ester functionality of the ligand **L**, resulting in the formation of a hexagonal chair shaped 0D hydrogen bonding synthon. This synthon was further stabilised by C=O···π [3.227(4)–3.336(8) Å] interactions involving C=O of the ester and aromatic functionalities of the ligand **L**. The supramolecular self-assembly of such 0D synthon leads to the formation of a 2D corrugated sheet-like architecture having a 3-c net honeycomb topology with Schläfli symbol {6³}. The C–H···F hydrogen bonding [C–H···F = 3.137(10)–3.195(4) Å, <C–H–F = 123–174°] comprising the C–H of pyrazole, pyridine, –CH₃ of pyrazole, –CH₂– spacer and –CH₂– of ester with BF₄⁻ anions facilitated the self-assembly of a 2D corrugated sheet, into a three dimensional hydrogen bonded network structure having a five nodal 1,3,3,3,7-c net with Schläfli symbol {0}{3.5.6}{3².5².6³.7³.8³.9²}{4.5.7}2 (Figure 4).

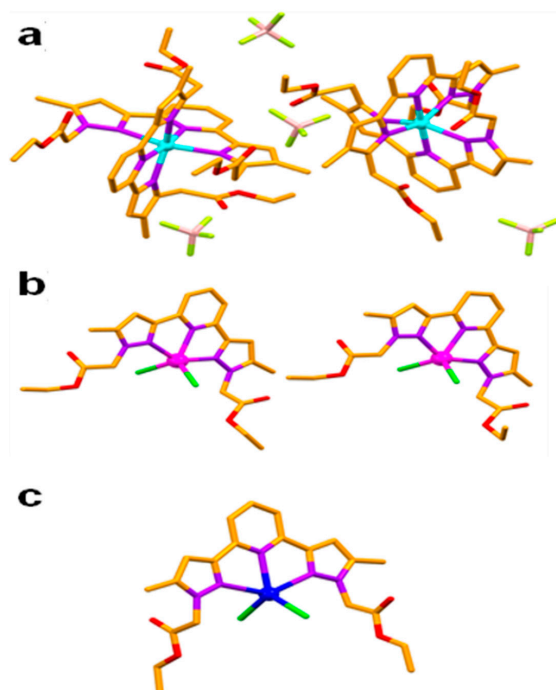


Figure 3. Asymmetric units of **1** (a), **2** (b) and **3** (c). (Hydrogen atoms were omitted for clarity, Colour code—C—orange, N—purple, O—red, Cl—green, Zn—cyan, Mn—magenta, Cd—brown.

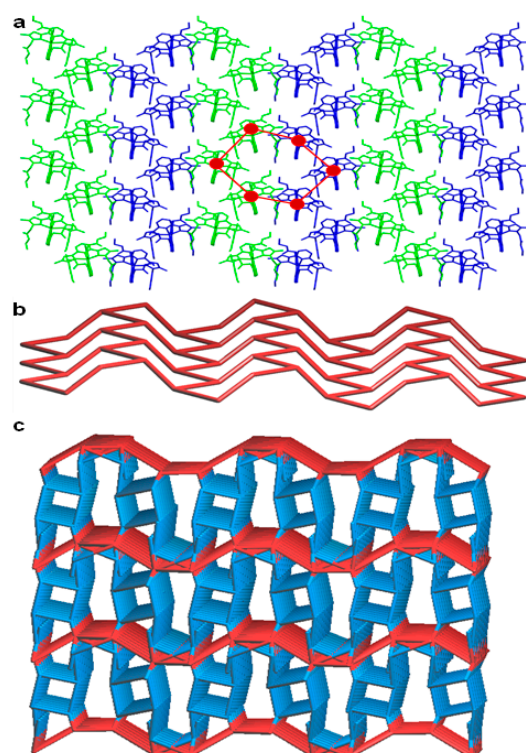


Figure 4. Crystal structure illustration of **1**—(a) 2D corrugated sheet like architecture formed by the self-assembly of crystallographically independent molecules (shown in green and blue colour capped stick model) of **1**, built from hexagonal chair shaped 0D hydrogen bonding synthon (red colour hexagon); (b) TOPOS view of 2D corrugated sheet having a 3-c net honeycomb topology; (c) TOPOS view [31,35] of the 3D hydrogen bonded network structure.

SXRD analysis revealed that single crystals of **2** belong to the centrosymmetric monoclinic space group $P2_1/c$. The asymmetric unit was comprised of two crystallographically independent molecules of coordination complex **2**. The coordination complex **2** consists of Mn(II) ion, two chloride anions and one ligand **L**. In the unit cell, there were four such units of each crystallographically independent molecules of **2**, which were symmetrically related by two-fold screw axis (2_1), glide plane and centre of inversion. The Mn(II) showed a distorted trigonal bipyramidal geometry [$\angle\text{N-Zn-N} = 70.8(2)\text{--}142.35(13)^\circ$; $\angle\text{N-Zn-Cl} = 96.37(10)\text{--}126.02(10)^\circ$; $\angle\text{N-Zn-Cl} = 112.45(5)\text{--}112.55(5)^\circ$], wherein the axial positions are coordinated by the N atom of the pyridine of ligand **L** and the chloride counter anions, whereas the apical positions are occupied with the N atoms of the pyrazole of **L**. The ligand **L** showed more planarity in **2** (considering only the aromatic portion of the **L**, the angle between the pyrazole rings of **L** were found to be $1.47\text{--}1.67^\circ$, which is smaller compared to the crystal structure of ligand **L** and **1**). Moreover, in the crystal structure, ligand **L** in both crystallographically independent coordination complexes displays *anti-syn-syn-syn-syn* conformation. The formation of pyrazole and ethyl acetate functionality in **L** was confirmed by the corresponding average bond lengths of N–N, C=O and C–O such as $1.328(7)\text{--}1.367(7)$ Å, $1.187(7)\text{--}1.209(8)$ Å, and $1.326(6)\text{--}1.330(6)$ Å, respectively. While one of the crystallographically independent molecules of **2** showed C–H \cdots O [C–H of pyridine and C=O of ester, C–H \cdots O = $3.204(9)$ Å, $\angle\text{C–H–O} = 125^\circ$] hydrogen bonding and other weak interactions resulted in the formation of a 2D hydrogen bonded sheet structure along the ‘bc’ plane, the second crystallographically independent molecule of **1** displayed C–H \cdots Cl [–CH₂– spacer and metal bound chloride, C–H \cdots Cl = $3.204(9)$ Å, $\angle\text{C–H–Cl} = 125^\circ$] hydrogen bonding which resulted in a 1D zigzag hydrogen bonded chain. Interestingly, these 1D zigzag hydrogen bonded chains (extended through ‘c’ axis) are packed on the top and bottom of the 2D sheet, with the support of C–H \cdots O [C–H \cdots O = $3.227(10)$ Å, $\angle\text{C–H–O} = 123^\circ$] hydrogen bonding involving –CH₂– ester and C=O group of ester functionality which resulted in a 3,4-c net with Schläfli symbol $\{5^2.8\}\{5^3.6^2.7\}$ (Figure 5).

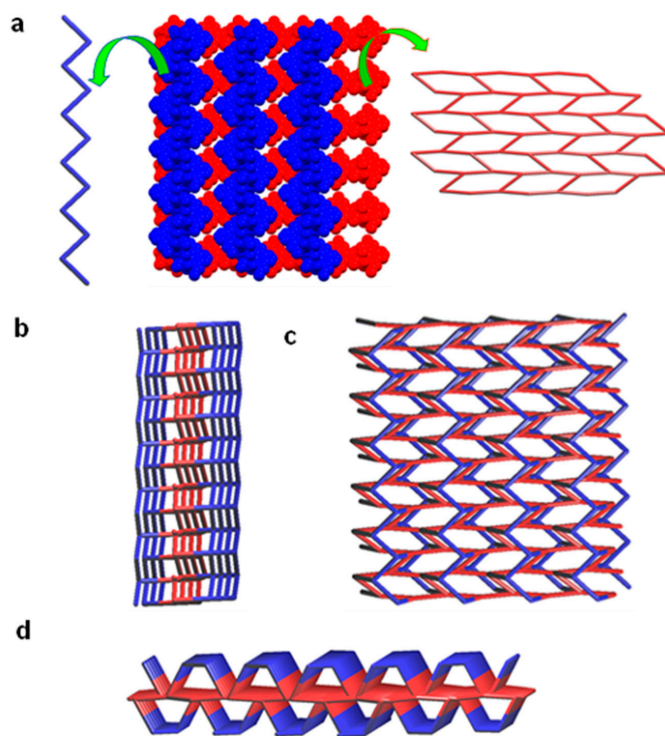


Figure 5. Crystal structure illustration of **2**—(a) packing of 1D zigzag hydrogen bonded chain (blue colour) over the 2D hydrogen bonded sheet structure along the ‘bc’ plane (red), TOPOS view [31,35] are shown in left and right side, respectively; (b–d) TOPOS view of packing of 1D zigzag hydrogen bonded chains on the top and bottom of the 2D sheet, along various crystallographic axis.

Coordination complex **3** crystallises in the centrosymmetric monoclinic space group $P2_1/n$. The asymmetric unit is comprised of one half of the molecule of **3**, i.e., one half of Cd(II) metal ion, one half of the molecule of **L** and one chloride anion (both **L** and chloride anions were coordinated to Cd(II)). The two-fold axis is passing through the Cd(II) metal centre and N(1) and C(1) atoms of the ligand **L**. Due to the presence of this two-fold axis, the remaining half of Cd(II), ligand **L** and chloride anion are generated by symmetry. In the crystal structure, the metal atom Cd(II) displays distorted trigonal bipyramidal geometry with angles ranging from $69.47(5)$ – $104.26(5)^\circ$. The axial coordination sites of Cd(II) were occupied by the two pyrazole nitrogen atoms of **L** whereas the equatorial sites are occupied by nitrogen atom of pyridine moiety of **L** and two chloride anions. Like in **2**, the ligand **L** showed *anti-syn-syn-syn-syn* conformation with slight non-planarity in **3**, which is revealed from the angle (6.33°) between the pyrazole rings. From the crystal structure, it is revealed that the bond lengths of N–N, C=O and C–O are $1.349(3)$ Å, $1.186(4)$ Å, and $1.320(4)$ Å, respectively, which confirmed the presence of pyrazole and ethyl acetate moieties in the ligand **L**. The supramolecular structure of **3** can be best called as a 2D hydrogen bonded sheet. The C–H \cdots O hydrogen bonding [C–H \cdots O = $3.258(6)$ Å, \angle C–H–O = 147°] involving the –CH₃ of the pyrazole ring and O = C of the ethyl acetate facilitate the formation of a 1D hydrogen bonded chain as the primary supramolecular structure. Furthermore, 2D hydrogen bonded sheet is built from the supramolecular self-assembly through C–H \cdots Cl hydrogen bonding [C–H \cdots Cl = $3.564(10)$ Å, \angle C–H–Cl = 133°] via the C–H of pyridine and metal bound chloride, along the crystallographic plane 'ab' (Figure 6).

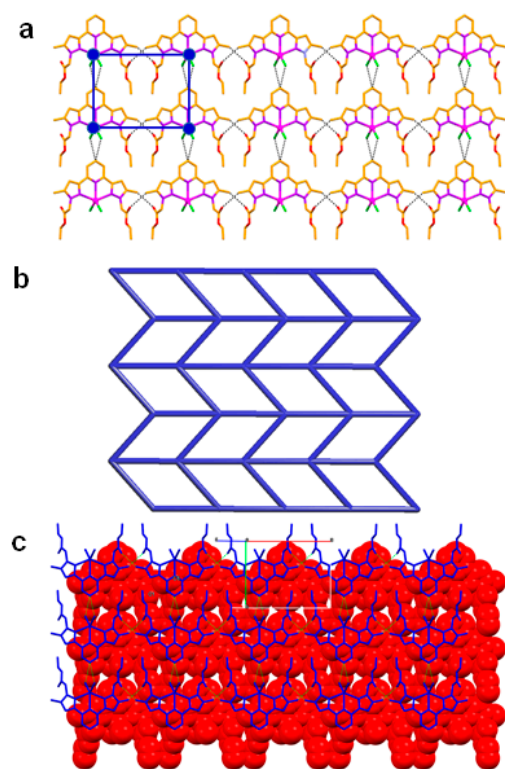


Figure 6. Crystal structure illustration of **3**—(a) 2D hydrogen bonded sheet; (b) TOPOS [31,35] view of 2D hydrogen bonded sheet; (c) offset packing of 2D sheets (adjacent sheets are shown in red colour spacefill model and blue colour capped stick model).

4. Discussions

4.1. Hirshfeld Surface Analyses

To investigate more about the supramolecular interactions in the crystal structures of **B**, **L**, **1**, **2** and **3**, Hirshfeld surfaces have been calculated for all the structures. From Hirshfeld surface [36] analysis, we can quantify various supramolecular interactions present in the

crystal structure. We used CRYSTAL EXPLORER [37] to plot the Hirshfeld surfaces [38] and calculate their respective 2D fingerprint plots [39].

The 3D maps of Hirshfeld surface (HS) assist us to find out the main interactions between molecules, and the 2D fingerprint plot (FP) help us to understand the distances among atoms involved in those interactions. More precisely, 3D HS and 2D FP enable us to give insights into qualitative and quantitative analysis of supramolecular interactions, respectively, present in the molecule. The 3D HS plots of **B**, **L**, **1**, **2** and **3** are presented in Figure 7, exhibiting the surface map over the normalised contact distance (d_{norm}), which can be determined from the d_e (the distance between the Hirshfeld surface and adjacent nucleus outside the surface), d_i (the distance between the Hirshfeld surface and nearest inside the nucleus) and the van der Waals radii of the atoms (r_i^{vdW} or r_e^{vdW}) from Equation (1):

$$d_{norm} = \frac{d_i - r_i^{vdw}}{r_i^{vdw}} + \frac{d_e - r_e^{vdw}}{r_e^{vdw}} \quad (1)$$

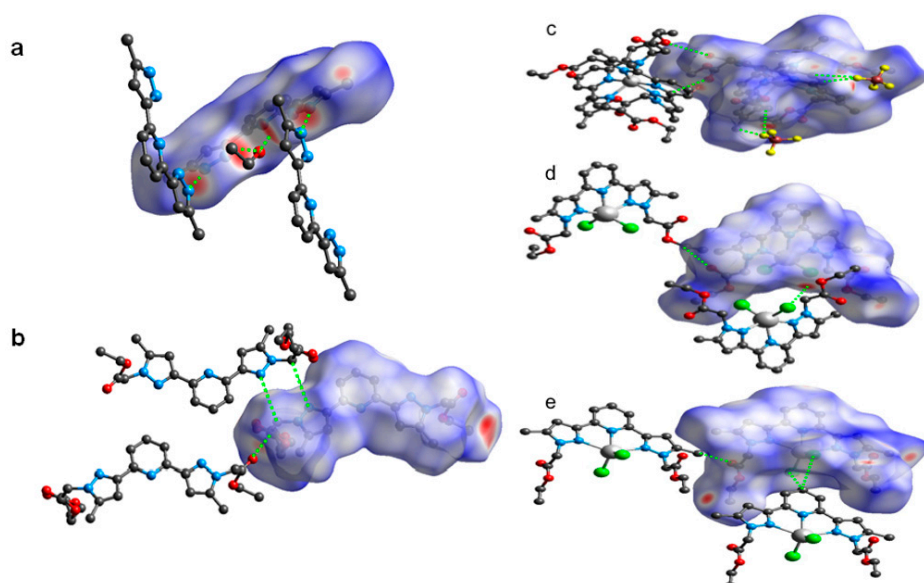


Figure 7. Views of the d_{norm} Hirshfeld surfaces of **B** (a) and **L** (b), displaying various interactions (shown in green colour dotted lines). Views of the d_{norm} Hirshfeld surfaces of **1** (c), **2** (d) and **3** (e), displaying various supramolecular interactions (shown in green colour dotted lines).

The corresponding shape index and curvedness of **B**, **L**, **1**, **2** and **3** are shown in Figures S1–S4 (ESI). In the d_{norm} map, the red spots indicate the closeness of atoms to the HS from outside, meaning a strong hydrogen bonding exists between the HS and the nearest atoms outside. While the white areas on the 3D HS designate the contacts with distances equal to the sum of van der Waals radii, the blue colour regions indicate the longer distances than the van der Waals radii as shown in Figure 7a,b. The HS of **B** was generated by using a standard (high) surface resolution with 3D d_{norm} surfaces mapped to a range -0.6557 to 1.3709 a.u. From the d_{norm} mapping, it is revealed that strong hydrogen bonding interactions such as $N-H\cdots N$ (between the pyrazole moieties) and $N-H\cdots O$ (between pyrazole and solvated ethanol) were present in the crystal lattice of **B**, as observed from the bright red spots on the HS. On the other hand, 3D d_{norm} surfaces mapping (ranges between -0.6823 to 1.4926 a.u.) of **L**, showed bright red spots near to $C=O$ of ester, pyrazole and $-CH_2-$ spacer of neighbouring molecules of **L**, confirming $C-H\cdots O$ and $C-H\cdots N$ hydrogen bonding interactions.

The contributions of the interatomic contacts ($C\cdots H$, $N\cdots H$, and $O\cdots H$) present in **B** and **L** are revealed from the 2D FP (Table 2). The $C\cdots H$ interatomic contacts present in **B**

and **L** are due to the C–H $\cdots\pi$ involving C–H of pyrazole and pyrazole ring, and C–H of spacer and pyridine ring, respectively. Weak $\pi\cdots\pi$ stacking (C \cdots C = 0.9%), lone pair $\cdots\pi$ (C \cdots O = 0.9%), and stacking of the aromatic rings (C \cdots N = 1.8%) were also present in the crystal structure of **L**.

Table 2. Contributions of the interatomic contacts (%) in the compounds presented in this paper.

	B (%)	L (%)	1 (%)	2 (%)	3 (%)
O \cdots H	2.5	13.9	13.8	14.5	15.8
N \cdots H	22.2	9.6	1.8	4.9	5.8
C \cdots H	25.9	14.9	8.9	10	10.9
H \cdots H	49.3	57.3	51.9	46.6	43.9
F \cdots H	–	–	21.1	–	–
Cl \cdots H	–	–	–	18.2	17.8
C \cdots C	0.1	0.9	–	2.7	3.1
Cl \cdots O	–	–	–	0.5	0.6
C \cdots O	–	0.9	2.0	–	–
N \cdots C	–	1.8	–	–	–

The HS mapped over d_{norm} of the coordination complexes **1**, **2** and **3** are in the range of -0.2538 to 1.6883 a.u., -0.2479 to 1.6747 a.u., -0.4067 to 1.4848 a.u., respectively (Figure 7c–e). The bright-red spots present on the 3D HS of **1**, **2** and **3** are due to the strong hydrogen bonding such as C–H \cdots O (C–H of pyridine and $-\text{CH}_2-$ of ester with C=O of the ester) and C–H \cdots F (C–H of aromatic rings, ester, and spacer with BF_4^- anion) interactions in **1**, C–H \cdots O (C–H of pyridine and C=O of the ester) and C–H \cdots Cl ($-\text{CH}_2-$ spacer and metal bound chloride) interactions in **2**, and C–H \cdots O ($-\text{CH}_3$ of the pyrazole ring and O = C of the ester) and C–H \cdots Cl (C–H of pyridine and metal bound chloride) interactions in **3**, as discussed in the crystal structure description (vide supra).

The resultant 2D FPs shown in Figures S5–S9 displayed the quantitative contribution of various intermolecular interactions present in their crystal structures of **1**, **2** and **3** (Table 2). The C \cdots H interatomic contacts were also present in the crystal structures of **1**, **2** and **3**, due to the C–H $\cdots\pi$ interactions (C–H of ester and pyrazole/pyridine ring in **1**, C–H of ester and pyrazole ring in **2**, and C–H of the methyl group of pyrazole/pyridine ring in **3**). Supramolecular interactions such as $\pi\cdots\pi$ stacking (C \cdots C = 2.7% in **2** and 3.1% in **3**), lone pair $\cdots\pi$ (C \cdots O = 2.0% in **1**) were also present in the crystal structures of the coordination complexes (Table 2). Weak Van der Waals interactions were also found in **2** and **3** (Cl \cdots O = 0.5% in **2** and 0.6% in **3**). Moreover, the H \cdots H contacts in **B**, **L**, **1**, **2** and **3** comprise of the major contributors to the contact list of 2D FP, such as 49.3%, 57.3%, 51.9%, 46.6% and 43.9%, respectively, within the HS. This is due to the high share of hydrogen atoms present in their crystal structures. Interestingly, the presence of sharp spikes was found in the 2D FPs of **1**, **2**, and **3**, which indicate the presence of strong C–H \cdots X ($d_i + d_e = 2.19$ Å, 2.48 Å, and 2.72 Å, for **1**, **2** and **3**, respectively, which have contributions of 21.1, 18.2 and 17.8%) and C–H \cdots O ($d_i + d_e = 2.47$ – 2.69 Å, 2.52 – 2.56 Å, and 2.29 – 2.73 Å, for **1**, **2** and **3**, respectively, which have contributions of 13.8, 14.5 and 15.8%) hydrogen bonding interactions, after considering the Cl \cdots H, F \cdots H and O \cdots H 2D FP, where X = F for **1**, and Cl for **2** and **3**. The contribution of H \cdots H, N \cdots H and C \cdots H interactions in the coordination complexes were decreased, compared to its ligand **L**, noticeably due to the presence of F \cdots H and Cl \cdots H interactions (Figure 8).

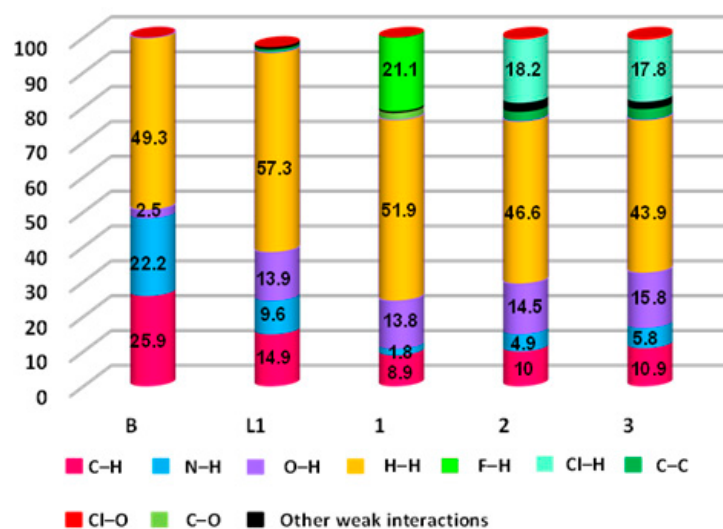


Figure 8. The relative contributions of all contacts present in **B**, **L**, **1**, **2** and **3**.

4.2. Influence of Counter-Anion and Metal Ion on the Conformation of the Ligand **L** and the Supramolecular Structures of the Coordination Complexes

The coordination complexes discussed herein showed supramolecular structural diversity in their crystal structures. The fundamental reason behind such diversity is due to the influence of various metal ions and counter anions, during the crystallisation process, which induced the conformational changes of the ligand **L** in the coordination complexes [40–42]. As shown in Scheme S1, there are several possible conformations of **L**, which can contribute to the coordination with metal ions. Indeed, due to the small energy barrier between various conformations of the flexible ligand **L**, it can display a particular conformation required for the coordination driven self-assembly of a metal ion. However, predicting such specific conformation is generally challenging, because of various hurdles such as the diversity in the possible orientations of the ligands in the crystals, the less precision in estimating the energies of ligand for its coordination with metal ion, and difficulty to predict the thermodynamic and kinetic contributions for the crystal growth. Hence, it is very important to recognise the supramolecular synthon present in the crystal structure, which is the sub-structural motif in the crystal.

The ligand **L** showed anti-anti-syn-anti-anti conformation in the crystal structure. Once it undergoes coordination with Zn(II) and form coordination complex **1**, the ligand **L** displayed two distinct conformations (two molecules of **L** are present in **1** such as syn-syn-syn-syn-syn and syn-syn-syn-syn-anti. The coordination geometry of Zn(II) and the BF_4^- anions present in the crystal lattice induce such conformations of **L**, in **1**. From the overlay structure of **L** with the **1** (Figure 9a,b), we can easily understand that the pyrazole rings of **L** rotate around 180° . Additionally, the self-assembly of **L** having these conformations, with the distorted octahedral Zn(II) via C–H \cdots O hydrogen bonding resulted in a hexagonal chair-shaped 0D hydrogen bonding synthon, the main sub-structural motif of **1**, which further extended into a 2D corrugated sheet structure through weak C=O \cdots π . In fact, the BF_4^- anions present in the crystal lattice of **1**, further assisted the self-assembly process via C–H \cdots F hydrogen bonding leading to the formation of a 3D hydrogen bonded network. On the other hand, **L** showed anti-syn-syn-syn-syn conformation in both **2** and **3**, where the counter anion is common, viz. chloride. In both coordination complexes **2** and **3**, chloride anions are coordinated to the metal ions. The difference between them is the metal ions, Mn(II) in **2** and Cd(II) in **3**, present in the coordination complex. Another clear difference is the presence of two crystallographically independent molecules of coordination complex in **2**, wherein in the case of **3**, only one molecule was present in the asymmetric unit. The difference in the ionic radius of Mn(II) (0.75 Å) and Cd(II) (0.87 Å) is one of the crucial factors for such variances.

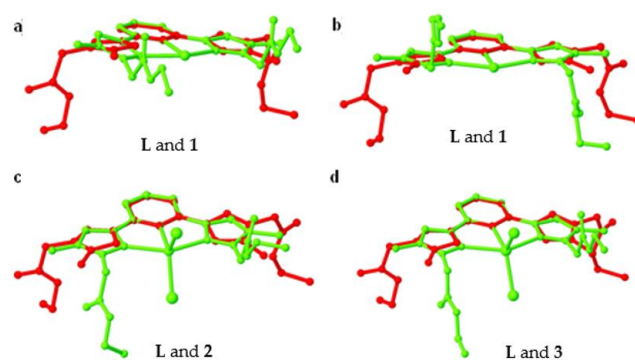


Figure 9. A molecular overlay of L with 1 (a) and (b), 2 (c), and 3 (d).

As a result, the primary supramolecular synthons of 2 and 3 were also different; while the crystallographically independent molecules of 2 showed hexagonal shaped supramolecular synthon through C–H···O, which further extended to a 2D hydrogen bonded sheet structure, the C–H···Cl interaction assisted the formation of a 1D zigzag hydrogen bonded chain (such chains are further packed top and bottom of the sheets). The C–H···O hydrogen bonding in 3 gives a 1D hydrogen bonded chain as the primary supramolecular structure, which further extended to a 2D hydrogen bonded sheet structure with the support of C–H···Cl interactions. From the overlay of the structure of 2 and 3 over the ligand L, a difference in the conformations is observed (Figure 9c,d). Although the conformation of L is identical in 2 and 3, the supramolecular packing is different due to the packing of the molecules induced by anion and metal ion as a result of symmetry difference.

We have investigated the thermal stability of L, and its coordination complexes, by thermo-gravimetric analysis (TGA) over the 25–900 °C under nitrogen atmosphere at a heating rate of 10 °C/min. As expected, the coordination complexes showed much higher thermal stability than the ligand L, with 230 °C, 310 °C and 270 °C, for 1, 2 and 3 respectively. Thus, their thermal stability can be ordered as follows: L < 1 < 3 < 2. While 1 showed a continuous one step thermal decomposition, 2 and 3 exhibited a three-step thermal degradation, with sharp profiles at steps one and two. The higher thermal stability of 2 is due to the presence of a higher quantity of C–H···Cl (18.2% in 2 compared to 17.8% in 3) and other weak interactions (46.6% in 2 compared to 43.9% in 3), as revealed from the 2D FPs and 3D HS. The lower stability of 1, compared to 2 and 3, is also revealed from the 2D FPs and 3D HS data; although 21.1% of strong C–H···F is present in 1, the quantity of C–H···O (13.8% in 1, 14.5% in 2, 15.8% in 3) and N–H···O (1.8% in 1, 4.9% in 2 and 5.8% in 3) in 1 is less, in contrast to 2 and 3. Moreover, the contributions from π ··· π stacking and anion··· π interactions which were present in 2 and 3 (Table 2), were absent in 1 (Figure 10).

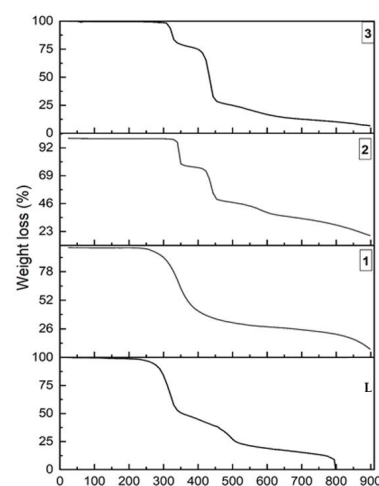


Figure 10. The thermo-gravimetric analysis (TGA) comparison plot of L, 1, 2 and 3.

5. Conclusions

A new flexible bis-pyrazol-bis-acetate ligand **L**, and its Zn(II), Mn(II) and Cd(II) coordination complexes have been synthesised and structurally characterised by single crystal X-ray diffraction. The ligand **L** showed diverse conformations once reacted with transition metals to produce the coordination complexes **1**, **2** and **3**. In addition, the intermediate compound **B**, which was found to be an achiral molecule, showed supramolecular chirality obtained from 2-fold rotational axes. While **L** showed a pair of 2D hydrogen bonded sheet structure having a 5-c net uninodal topology, **1** exhibited a 2D corrugated sheet like architecture having a honeycomb topology which further extended into a 3D hydrogen bonded network structure. Interestingly, two distinct topologies were observed in **2**, due to the presence of crystallographically independent molecules of **2** in the unit cell, namely a 2D hydrogen bonded sheet structure along the 'bc' plane and 1D zigzag hydrogen bonded chains, which are packed on the top and bottom of the 2D sheet. Finally, **3** showed a 2D hydrogen bonded sheet structure. Thus, the influence of the counter anions in shaping up the coordination modes of the metal ions and the conformation of ligand, resulting in various supramolecular synthons which control the self-assembly of coordination complexes, was demonstrated. Remarkably, **1**, **2** and **3** showed unusual thermal stability as revealed from thermogravimetric analyses, which can be justified by the presence of strong supramolecular interactions, as revealed by the crystal structure and Hirshfield surface analyses. Its unique thermal stability could provide stable hybrid materials upon grafting **L** to silica for metallic decontamination purposes, particularly towards Zn(II), Mn(II) and Cd(II) which are recognised as toxic metal ions. This technology is currently under investigation in our laboratory and already applied to real water samples (e.g., from natural rivers) [43–52].

Supplementary Materials: The following are available online at <https://www.mdpi.com/2071-1050/13/1/288/s1>, This section contains crystallographic information, NMR, ESI-MS, FT-IR and UV-vis spectra and TGA.

Author Contributions: The following statements should be used Conceptualisation, S.R. and Y.G.; methodology, S.R. and Y.G.; crystallography, H.N.M. and N.N.A.; synthesis and characterisation, A.O.; writing—original draft preparation, S.R., A.O., H.N.M., N.N.A. and Y.G.; supervision, Y.G. and S.R.; project administration, Y.G. and S.R.; funding acquisition, Y.G. and S.R. All authors have read and agreed to the published version of the manuscript.

Funding: This research was supported by a bilateral WBI-Morocco grant (COP 22 Program 2018–2022), the Fonds De La Recherche Scientifique—FNRS (CDR 33694457, PDR T.0095.21) and PPR2-MESRSFC-CNRST-P10 project (Morocco). We thank both WBI-Morocco for an excellence PhD stipendium and UCLouvain international action committee for a PhD scholarship allocated to A.O.

Institutional Review Board Statement: Not applicable.

Informed Consent Statement: Not applicable.

Data Availability Statement: Not applicable.

Acknowledgments: We thank K. Robeyns for generating the cif files of **B** and **L**.

Conflicts of Interest: There are no conflict to declare.

References

1. Adarsh, N.N.; Dastidar, P. Coordination polymers: What has been achieved in going from innocent 4,4'-bipyridine to bis-pyridyl ligands having a non-innocent backbone? *Chem. Soc. Rev.* **2012**, *41*, 3039–3060. [[CrossRef](#)] [[PubMed](#)]
2. Smulders, M.M.J.; Riddell, I.A.; Browne, C.; Nitschke, J.R. Building on architectural principles for three-dimensional metallo-supramolecular construction. *Chem. Soc. Rev.* **2013**, *42*, 1728–1754. [[CrossRef](#)] [[PubMed](#)]
3. Lu, J.; Duriska, M.B.; Neville, S.M.; Iremonger, S.S.; Boas, J.F.; Kepert, C.J.; Batten, S.R. Systematic Metal Variation and Solvent and Hydrogen-Gas Storage in Supramolecular Nanoballs. *Angew. Chem. Int. Ed.* **2009**, *48*, 8919–8922. [[CrossRef](#)]
4. Chakrabarty, R.; Mukherjee, P.S.; Stang, P. Supramolecular Coordination: Self-Assembly of Finite Two- and Three-Dimensional Ensembles. *Chem. Rev.* **2011**, *111*, 6810–6918. [[CrossRef](#)]

5. Domoto, Y.; Abe, M.; Kikuchi, T.; Fujita, M. Self-Assembly of Coordination Polyhedra with Highly Entangled Faces Induced by Metal–Acetylene Interactions. *Angew. Chem. Int. Ed.* **2020**, *59*, 3450–3454. [[CrossRef](#)]
6. Janiak, C.; Vieth, J.K. MOFs, MILs and more: Concepts, properties and applications for porous coordination networks (PCNs). *New J. Chem.* **2010**, *34*, 2366–2388. [[CrossRef](#)]
7. Aakeröy, C.B.; Champness, N.R.; Janiak, C. Recent advances in crystal engineering. *CrystEngComm* **2009**, *12*, 22–43. [[CrossRef](#)]
8. Adarsh, N.N.; Dîrtu, M.M.; Guionneau, P.; Devlin, E.; Sanakis, Y.; Howard, J.A.K.; Chattopadhyay, B.; Garcia, Y. One-Dimensional Looped Chain and Two-Dimensional Square Grid Coordination Polymers: Encapsulation of Bis(1,2,4-Triazole)-trans-cyclohexane into the Voids. *Eur. J. Inorg. Chem.* **2019**, *2019*, 585–591. [[CrossRef](#)]
9. Paul, M.; Adarsh, N.N.; Dastidar, P. Cu^{II} Coordination Polymers Capable of Gelation and Selective SO₄²⁻ Separation. *Cryst. Growth Des.* **2012**, *12*, 4135–4143. [[CrossRef](#)]
10. Neumann, T.; Gallo, G.; Dinnebier, R.E.; Näther, C. Synthesis, Crystal Structures, and Properties of Mn(NCS)₂ Coordination Compounds with 4-Picoline as Coligand and Crystal Structure of Mn(NCS)₂. *Z. Anorg. Allg. Chem.* **2020**, *646*, 88–94. [[CrossRef](#)]
11. Caillé, F.; Bonnet, C.S.; Buron, F.; Villette, S.; Helm, L.; Petoud, S.; Suzenet, F.; Tóth, É. Isoquinoline-Based Lanthanide Complexes: Bright NIR Optical Probes and Efficient MRI Agents. *Inorg. Chem.* **2012**, *51*, 2522–2532. [[CrossRef](#)] [[PubMed](#)]
12. Adarsh, N.N.; Novio, F.; Ruiz-Molina, D. Coordination polymers built from 1,4-bis(imidazol-1-ylmethyl)benzene: From crystalline to amorphous. *Dalton Trans.* **2016**, *45*, 11233–11255. [[CrossRef](#)] [[PubMed](#)]
13. Viciano-Chumillas, M.; Tanase, S.; De Jongh, L.J.; Reedijk, J. Coordination Versatility of Pyrazole-Based Ligands towards High-Nuclearity Transition-Metal and Rare-Earth Clusters. *Eur. J. Inorg. Chem.* **2010**, *2010*, 3403–3418. [[CrossRef](#)]
14. Batten, S.R.; Duriska, M.B.; Jensen, P.; Lu, J. Synthesis and Complexes of the New Scorpionate Ligand Tris[3-(4-benzonitrile)-pyrazol-1-yl]borate. *Aust. J. Chem.* **2007**, *60*, 72–74. [[CrossRef](#)]
15. Ogryzek, M.; Chylewska, A.; Królicka, A.; Banasiuk, R.; Turecka, K.; Lesiak, D.; Nidzworski, D.; Makowski, M. Coordination chemistry of pyrazine derivatives analogues of PZA: Design, synthesis, characterization and biological activity. *RSC Adv.* **2016**, *6*, 52009–52025. [[CrossRef](#)]
16. Radi, S.; Yahyi, A.; Ettouhami, A.; Jha, A.C.; Adarsh, N.N.; Robeyns, K.; Garcia, Y. Synthesis and crystal structures of mononuclear Cu^{II}/Co^{II} coordination complexes from pyrazole-dicarboxylate acid derivatives. *Polyhedron* **2015**, *85*, 383–388. [[CrossRef](#)]
17. Radi, S.; El-Massaoudi, M.; Benaissa, H.; Adarsh, N.N.; Ferbinteanu, M.; Devlin, E.; Sanakis, Y.; Garcia, Y. Crystal engineering of a series of complexes and coordination polymers based on pyrazole-carboxylic acid ligands. *New J. Chem.* **2017**, *41*, 8232–8241. [[CrossRef](#)]
18. El-Massaoudi, M.; Radi, S.; Mabkhot, Y.N.; Al-Showiman, S.; Ghabbour, H.A.; Ferbinteanu, M.; Adarsh, N.N.; Garcia, Y. Cu(II) and Mn(II) coordination complexes constructed by C linked bispyrazoles: Effect of anions and hydrogen bonding on the self assembly process. *Inorganica Chim. Acta* **2018**, *482*, 411–419. [[CrossRef](#)]
19. Chkirate, K.; Fettach, S.; Karrouchi, K.; Sebbar, N.K.; Essassi, E.M.; Mague, J.T.; Radi, S.; Faouzi, M.E.A.; Adarsh, N.N.; Garcia, Y. Novel Co(II) and Cu(II) coordination complexes constructed from pyrazole-acetamide: Effect of hydrogen bonding on the self assembly process and antioxidant activity. *J. Inorg. Biochem.* **2019**, *191*, 21–28. [[CrossRef](#)]
20. Chkirate, K.; Karrouchi, K.; Dege, N.; Sebbar, N.K.; Ejjoummany, A.; Radi, S.; Adarsh, N.N.; Talbaoui, A.; Ferbinteanu, M.; Essassi, E.M.; et al. Co(ii) and Zn(ii) pyrazolyl-benzimidazole complexes with remarkable antibacterial activity. *New J. Chem.* **2020**, *44*, 2210–2221. [[CrossRef](#)]
21. Zhang, X.; Xing, N.; Bai, F.-Y.; Wan, L.; Shan, H.; Hou, Y.; Xing, Y.; Shi, Z. Multi-functional d10 metal–organic materials based on bis-pyrazole/pyridine ligands supported by a 2,6-di(3-pyrazolyl)pyridine with different spanning flexible dicarboxylate ligands: Synthesis, structure, photoluminescent and catalytic properties. *CrystEngComm* **2013**, *15*, 9135–9147. [[CrossRef](#)]
22. Miao, L.-L.; Li, H.-X.; Yu, M.; Zhao, W.; Gong, W.-J.; Gao, J.; Ren, Z.-G.; Wang, H.-F.; Lang, J.-P. Preparation of a nitrate-coordinated copper(II) complex of 2-(pyrazol-3-yl)-6-(pyrazolate)pyridine as an efficient catalyst for methyl methacrylate polymerization. *Dalton Trans.* **2012**, *41*, 3424–3430. [[CrossRef](#)] [[PubMed](#)]
23. Shin, M.S.; Oh, B.J.; Ryu, J.Y.; Park, M.H.; Kim, M.; Lee, J.; Kim, Y. Synthesis, characterization, and cycloaddition reaction studies of zinc(II) acetate complexes containing 2,6-bis(pyrazol-1-yl)pyridine and 2,6-bis(3,5-dimethylpyrazol-1-yl)pyridine ligands. *Polyhedron* **2017**, *125*, 101–106. [[CrossRef](#)]
24. Khmara, E.F.; Chizhov, D.L.; Sidorov, A.A.; Aleksandrov, G.G.; Slepukhin, P.A.; Kiskin, M.A.; Tokarev, K.L.; Filyakova, V.I.; Rusinov, G.L.; Smolyaninov, I.V.; et al. Synthesis, structure, electrochemical and magnetic properties of 2,6-bis(5-trifluoromethylpyrazol-3-yl)pyridine and its Ni^{II} complexes. *Russ. Chem. Bull.* **2012**, *61*, 313–325. [[CrossRef](#)]
25. Jornet-Mollá, V.; Waerenborgh, J.C.; Romero, F.M. Synthesis, Structure, and Photomagnetic Properties of a Hydrogen-Bonded Lattice of [Fe(bpp)₂]²⁺ Spin-Crossover Complexes and Nicotinate Anions. *Crystals* **2018**, *8*, 439. [[CrossRef](#)]
26. Guan, Q.-L.; Liu, Z.; Wei, W.-J.; Xing, Y.-H.; Liu, J.; Zhang, R.; Hou, Y.-N.; Wang, X.; Bai, F.-Y. Synthesis, structure, spectroscopy of four novel supramolecular complexes and cytotoxicity study by application of multiple parallel perfused microbioreactors. *New J. Chem.* **2014**, *38*, 3258–3268. [[CrossRef](#)]
27. Berdiell, I.C.; Kulmaczewski, R.; Halcrow, M.A. Iron(II) Complexes of 2,4-Dipyrazolyl-1,3,5-triazine Derivatives—The Influence of Ligand Geometry on Metal Ion Spin State. *Inorg. Chem.* **2017**, *56*, 8817–8828. [[CrossRef](#)]
28. Ojwach, S.O.; Nyamato, G.S.; Omondi, B.; Darkwa, J.; Okoth, A.O. Multidentate bis(pyrazolylmethyl)pyridine ligands: Coordination chemistry and binding properties with zinc(II) and cadmium(II) cations. *J. Coord. Chem.* **2012**, *65*, 298–307. [[CrossRef](#)]
29. Sheldrick, G.M. Phase annealing in SHELX-90: Direct methods for larger structures. *Acta Crystallogr. A* **1990**, *46*, 467–473. [[CrossRef](#)]

30. Sheldrick, G. A short history of SHELX. *Acta Crystallogr. A* **2008**, *64*, 112–122. [[CrossRef](#)]
31. Farrugia, L.J. WinGX suite for small-molecule single-crystal crystallography. *J. Appl. Crystallogr.* **1999**, *32*, 837–838. [[CrossRef](#)]
32. Clark, R.C.; Reid, J.S. The analytical calculation of absorption in multifaceted crystals. *Acta Crystallogr. A* **1995**, *51*, 887–897. [[CrossRef](#)]
33. Miyata, M.; Tohnai, N.; Hisaki, I.; Sasaki, T. Generation of Supramolecular Chirality around Twofold Rotational or Helical Axes in Crystalline Assemblies of Achiral Components. *Symmetry* **2015**, *7*, 1914–1928. [[CrossRef](#)]
34. Dîrtu, M.M.; Adarsh, N.N.; Naik, A.D.; Robeyns, K.; Garcia, Y. Supramolecular homochiral helicity and zigzag hydrogen bonded chains in 1,2,4-triazole derived aminoester and aminoacid. *New J. Chem.* **2016**, *40*, 9025–9029. [[CrossRef](#)]
35. Blatov, V.A.; Shevchenko, A.P.; Proserpio, D.M. Applied Topological Analysis of Crystal Structures with the Program Package ToposPro. *Cryst. Growth Des.* **2014**, *14*, 3576–3586. [[CrossRef](#)]
36. Spackman, M.A.; Jayatilaka, D. Hirshfeld surface analysis. *CrystEngComm* **2008**, *11*, 19–32. [[CrossRef](#)]
37. Turner, M.J.; McKinnon, J.J.; Wolff, S.K.; Grimwood, D.J.; Spackman, P.R.; Jayatilaka, D.; Spackman, M.A. Hirshfeld surfaces and two-dimensional fingerprint plots were generated by using CrystalExplorer17. In *Crystal Explorer17*; University of Western Australia: Crawley, Australia, 2017.
38. Hirshfeld, H.L. Synthesis, Crystal structure, and Hirshfeld Surface Analysis of a New Mixed Ligand Copper (II) Complex. *Theor. Chim. Acta.* **1977**, *44*, 129–138. [[CrossRef](#)]
39. McKinnon, J.J.; Jayatilaka, D.; Spackman, M.A. Towards quantitative analysis of intermolecular interactions with Hirshfeld surfaces. *Chem. Commun.* **2007**, 3814–3816. [[CrossRef](#)]
40. Adarsh, N.N.; Kumar, D.K.; Dastidar, P. Ligating topology and counter anion controlled formation of discrete metallo-macrocyclic and 2D corrugated sheet in coordination compounds derived from a bis-pyridyl-bis-amide ligand and Cd (II) salts. *Inorg. Chem. Commun.* **2008**, *11*, 636–642. [[CrossRef](#)]
41. Deng, H.-Y.; He, J.-R.; Pan, M.; Li, L.; Su, C.-Y. Synergistic metal and anion effects on the formation of coordination assemblies from a *N,N'*-bis(3-pyridylmethyl)naphthalene diimide ligand. *CrystEngComm* **2009**, *11*, 909–917. [[CrossRef](#)]
42. Adarsh, N.N.; Kumar, D.K.; Suresh, E.; Dastidar, P. Coordination polymers derived from a bis-pyridyl-bis-amide ligand: Supramolecular structural diversities and anion binding properties. *Inorganica Chim. Acta* **2010**, *363*, 1367–1376. [[CrossRef](#)]
43. Radi, S.; Toubi, Y.; Bacquet, M.; Degoutin, S.; Mabkhot, Y.N.; Garcia, Y. An inorganic–organic hybrid material made of a silica-immobilized Schiff base receptor and its preliminary use in heavy metal removal. *RSC Adv.* **2016**, *6*, 34212–34218. [[CrossRef](#)]
44. Radi, S.; Tighadouini, S.; Bacquet, M.; Degoutin, S.; Garcia, Y. New hybrid material based on a silica-immobilized conjugated β -ketoenol-bipyridine receptor and its excellent Cu(II) adsorption capacity. *Anal. Methods* **2016**, *8*, 6923–6931. [[CrossRef](#)]
45. Radi, S.; El-Massaoudi, M.; Bacquet, M.; Degoutin, S.; Adarsh, N.N.; Robeyns, K.; Garcia, Y. A novel environment-friendly hybrid material based on a modified silica gel with a bispyrazole derivative for the removal of Zn^{II}, Pb^{II}, Cd^{II} and Cu^{II} traces from aqueous solutions. *Inorg. Chem. Front.* **2017**, *4*, 1821–1831. [[CrossRef](#)]
46. El-Massaoudi, M.; Radi, S.; Bacquet, M.; Degoutin, S.; Garcia, Y. Highly efficient and selective adsorbent for potentially toxic metals removal from aquatic media. *J. Environ. Chem. Eng.* **2018**, *6*, 5980–5989. [[CrossRef](#)]
47. Tighadouini, S.; Radi, S.; Elidrissi, A.; Haboubi, K.; Bacquet, M.; Degoutin, S.; Zaghrioui, M.; Garcia, Y. Removal of toxic heavy metals from river water samples using a porous silica surface modified with a new β -ketoenolic host. *Beilstein J. Nanotechnol.* **2019**, *10*, 262–273. [[CrossRef](#)]
48. Tighadouini, S.; Radi, S.; Ferbinteanu, M.; Garcia, Y. Highly Selective Removal of Pb(II) by a Pyridylpyrazole- β -ketoenol Receptor Covalently Bonded onto the Silica Surface. *ACS Omega* **2019**, *4*, 3954–3964. [[CrossRef](#)]
49. Tighadouini, S.; Radi, S.; El Massaoudi, M.; Lakbaibi, Z.; Ferbinteanu, M.; Garcia, Y. Efficient and Environmentally Friendly Adsorbent Based on β -Ketoenol-Pyrazole-Thiophene for Heavy-Metal Ion Removal from Aquatic Medium: A Combined Experimental and Theoretical Study. *ACS Omega* **2020**, *5*, 17324–17336. [[CrossRef](#)]
50. Tighadouini, S.; Radi, S.; Elidrissi, A.; Zaghrioui, M.; Garcia, Y. Selective Confinement of Cd^{II} in Silica Particles Functionalized with β -Keto-Enol-Bisfuran Receptor: Isotherms, Kinetic and Thermodynamic Studies. *Eur. J. Inorg. Chem.* **2019**, *2019*, 3180–3186. [[CrossRef](#)]
51. Tighadouini, S.; Radi, S.; Garcia, Y. Selective chemical adsorption of Cd(II) on silica covalently decorated with a β -ketoenol-thiophene-furan receptor. *Mol. Syst. Des. Eng.* **2020**, *5*, 1037–1047. [[CrossRef](#)]
52. El-Massaoudi, M.; Radi, S.; Lamsayah, M.; Tighadouini, S.; Séraphin, K.K.; Kouassi, L.K.; Garcia, Y. Ultra-fast and highly efficient hybrid material removes Cu(II) from wastewater: Kinetic study and mechanism. *J. Clean. Prod.* **2021**, 124757. [[CrossRef](#)]